

# Quantum key distribution over a metropolitan network using an integrated photonics based prototype

Maria Ana Pereira,<sup>1</sup> Giulio Gualandi,<sup>2,3</sup> Rebecka Sax,<sup>1</sup> Alberto Boaron,<sup>1</sup> Raphaël Houlmann,<sup>1</sup> Roberto Osellame,<sup>2,3</sup> Rob Thew,<sup>1</sup> and Hugo Zbinden<sup>1</sup>

<sup>1)</sup>*Quantum Technologies Group, Department of Applied Physics, Université de Genève, Switzerland*

<sup>2)</sup>*Dipartimento di Fisica- Politecnico di Milano, piazza Leonardo da Vinci 32, 20133 Milano (Italy)*

<sup>3)</sup>*Istituto di Fotonica e Nanotecnologie- Consiglio Nazionale delle Ricerche (IFN-CNR), piazza Leonardo da Vinci 32, 20133 Milano (Italy).*

(\*Electronic mail: maria.dematosafonsopereira@unige.ch)

(Dated: February 20, 2026)

An industrial-scale adoption of Quantum Key Distribution (QKD) requires the development of practical, stable, resilient and cost-effective hardware that can be manufactured at large scales. In this work we present a high-speed (1.25GHz), field-deployable QKD prototype based on integrated photonics, that is consolidated into standard 19-inch rack compatible units. Through integrated photonics, the system prioritizes autonomous long-term stability in metropolitan settings. The architecture is further simplified by removing the need for chromatic dispersion compensation over metropolitan distances (below 100km). We demonstrate continuous key exchange over more than 4 km of metropolitan optical fiber, where the prototype maintained stable, uninterrupted operation across a measurement spanning more than 12 day-night cycles without manual intervention.

## I. INTRODUCTION

Although QKD has been established as a standard for information-theoretic security for more than two decades<sup>1</sup>, its widespread adoption across networks has been constrained by hardware limitations, as traditional QKD implementations rely on bulky, expensive components that are difficult to scale within dense telecommunication environments. Consequently, for over a decade, the focus has shifted from fundamental protocol demonstrations to the realization of scalable architectures<sup>2</sup>. Among the various approaches to address these scalability challenges, Photonic Integrated Circuits (PICs) have emerged as a promising solution by allowing the consolidation of multiple optical components on a single sub-centimeter chip, eliminating the need for discrete bulk optical components that are sensitive to mechanical perturbations and thermal gradients. The resulting compact form factor and low-power consumption (order of mW) allow the implementation of more practical and environmentally robust modules suitable for real-world telecommunications infrastructure<sup>3</sup>.

In this paper, we present the design, implementation and characterization of a PIC based, field-deployable QKD system based on time-bin encoding. Our system was designed with scalability, manufacturing efficiency and cost in mind. Using standardized footprints for the receiver and transmitter, it can accommodate a wide range of link distances and losses. The system has successfully performed key exchanges on more than 4km of metropolitan optical fiber with stable operation tested for around 12 day-night cycles.

### A. Overview of the QKD System

The protocol used in this work is the two-detector 3-state time-encoded BB84 with one decoy state<sup>4</sup>. The full secu-

rity analysis of the protocol used is detailed in the works of Rusca<sup>5,6</sup>. The prototype implementing this protocol is shown in Fig.1.

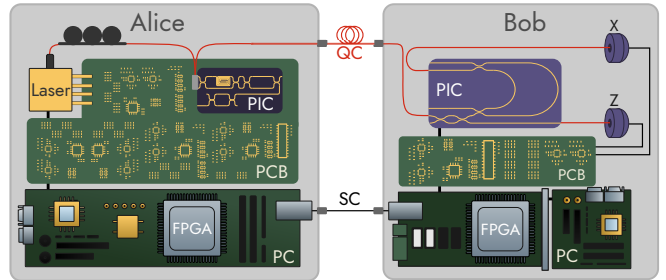


Figure 1: Schematic of the QKD system between a transmitter, Alice, and a receiver, Bob. Optically, Alice's setup includes a laser source, a polarization controller and a photonic integrated chip (PIC). The quantum channel (QC) transmits the quantum states to Bob that consists of a PIC and single-photon detectors (Z and X-basis measurements). Both parties are supported by printed circuit boards (PCB), personal computers (PC) and Field-Programmable Gate Arrays (FPGA) for control and processing, and utilize a service channel (SC) for clock synchronization basis reconciliation, error correction, and privacy amplification

The prototype is divided into two main parts: Alice's transmitter unit, consisting of a gain-switched laser, a polarization controller, the transmitter integrated chip, a custom electronic board, and a computer with an integrated Field Programmable Gate Array (FPGA) chip; and Bob's receiver, comprising the receiver integrated chip, two avalanche single-photon detectors, custom electronic board, a computer and an FPGA. The transmitter fits within a 1U 19-inch rack box while the receiver fits within a 3U 19-inch rack box. The additional 2U height is required to accommodate the 90-degree connection

between the FPGA (*AMD Kintex KC705 Evaluation Kit*) and the computer.

Building on the foundational PIC-based QKD experiment of Sax<sup>7</sup>, we introduced design improvements that transformed the integrated photonics systems from a proof-of-principle demonstration into a deployable prototype, with both the transmitter and receiver units redesigned with an emphasis on integration and miniaturization. The transmitter merged clock generation, RF-signal generation, laser driving circuitry, power supplies, and temperature control into a single Printed Circuit Board (PCB). At the receiver, detector units were significantly scaled down, shifting from a Stirling-cooler implementation ( $2.3 \times 10^{-2} \text{m}^3$ ) to a peltier-cooled approach ( $4.6 \times 10^{-4} \text{m}^3$ ).

We also reduced the system's operating frequency to 1.25GHz (from 2.5GHz<sup>7</sup>) to mitigate the effects of chromatic dispersion. At 1.25GHz each time-bin is 400ps rather than 200ps, making the measurement less susceptible to dispersion-induced temporal broadening (for the same laser temporal profile) which in turn enhances the state fidelity, as well as reducing the system's sensitivity to detector jitter. By making the system more dispersion-tolerant, we eliminate the need to design and adjust the length of Dispersion Compensating Fiber (DCF) for any given distance.

## II. TRANSMITTER PROTOTYPE

A custom PCB was designed in house with all the necessary electronics for the optical control of the prototype. The power distribution to the transmitter unit is managed in this PCB through a multirail power supply system that converts an initial 12V input into the various voltages required by the components. An FPGA interface stage converts the differential signals from the FPGA to single-ended SMA outputs to be used as the laser clock and an auxiliary clock. The laser clock features a programmable delay of up to 100ps in steps of 3ps that allows the user to precisely align temporally the optical pulse train and the electronic modulation signal.

The laser used is a high-bandwidth distributed feedback laser (Gooch & Housego's AA0701 series) operating at a wavelength of 1550.12nm at 25°C. It is mounted directly on the control PCB that provides both the DC bias current and the processed Radio Frequency (RF) FPGA clock signal (converted to single-end and amplified) that is used as a modulation signal to generate the gain-switched optical pulses.

The PIC and Electronic Integrated Circuit (EIC) are maintained at 40°C using a Peltier cooling stage controlled by a Thermo Electric Cooler (TEC) controller (MTD415T). A microcontroller serves as the central control hub, supplying current to the PIC heaters and interfacing with the EIC to provide the control signals for parameter adjustment in the Intensity Modulator (IM).

### A. Integrated Transmitter

The integrated transmitter comprises a PIC and an auxiliary EIC, both fabricated using standard silicon photonic technology and designed by Sicoya GmbH. Details of the fabrication are provided in Sax<sup>7</sup>. The fabricated chips had footprints of 4.50mm × 1.10mm and 4.50mm × 0.75mm (PIC and EIC respectively).

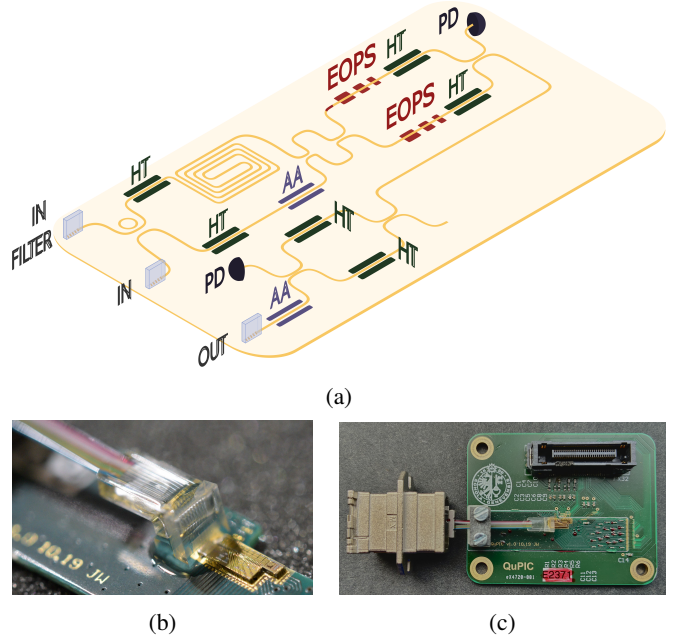


Figure 2: Pictures and schematics of the integrated transmitter. a) Schematic of the photonic integrated circuit of Alice showing the optical signal path. HT – Heaters; EOPS – electro-optic phase shifter; MZI – Mach-Zehnder interferometer; IM – intensity modulator; AA – absorption attenuator; PD – photodetectors. b) 90-degree fiber array used for optical coupling with PIC. c) PIC interposer PCB glued to SPI interface PCB.

The two chips are mounted on a custom interposer PCB. The interposer is glued and bonded to a larger PCB that interfaces with the remaining controlling electronics via a *PCIe X4* connector Fig. 2c. The EIC is directly bonded to the PIC and integrates multiple SPI-controlled, high-speed differential driver channels that provide digitally tunable gain, bandwidth equalization, and up to  $3V_{pp}$  output swing. The interposer also supports a 90-degree fiber array for optical coupling as seen in Fig. 2b. This light is coupled from this fiber array to and from chip using a grating coupler. An in-line polarization controller ( $7.5 \times 2.5 \times 4.0 \text{ cm}$ ), upstream of the chip, aligns the incoming polarization to maximize coupling efficiency.

The transmitter PIC, shown in Fig. 2a, consists of three main functional blocks: an unbalanced Mach-Zehnder interferometer (MZI) for qubit generation, an IM for state encoding and a variable attenuator for mean photon number setting.

**Spectral Cleaning:** A ring resonator (ring filter) on chip, in a filtering configuration, is a wavelength-selective optical

cavity coupled to two straight bus waveguides, an input bus and an output *drop* port. The light that propagates in the input bus couples evanescently into the ring only when the round-trip phase shift is an integer multiple of  $2\pi$ . This resonance condition is satisfied at specific resonant wavelengths ( $\lambda_{res} = 1550.9$ ). Our integrated ring filter linewidth was measured to be 0.170nm. The frequency linewidth was characterized by sweeping an optical filter (JDSU TB9) across the laser spectrum while measuring the Superconducting Nanowire Single Photon Detector (SNSPD) count rate.

**Qubit Generation:** The unbalanced MZI generates the coherent *early-late* pulse pairs with a 400ps delay, corresponding to a 3cm optical path difference ( $n_g = 4$ ); a notable achievement for on-chip silicon photonics integration. The MZI consists of an input  $1 \times 2$  Beam Splitter (BS), two arms with a 400ps delay and an output  $2 \times 1$  BS. Thermo-Optical Phase-Shifters (TOPSs) in both arms control the relative phase, while an Electronic Variable Optical Attenuator (EVOA), in the short arm, compensates for propagation losses accumulated in the long arm, improving interference visibility. The TOPSs rely on the thermo-optic effect to modulate the refractive index of the waveguide, whereas EVOAs exploit the free-carrier absorption effect in silicon to provide electrically controllable optical attenuation. All the aforementioned BSs used on chip are Multimode Interference-based.

**State encoding:** The IM encodes the quantum states at 2.5GHz (twice the laser's repetition rate). It uses a balanced MZI with three Electro-Optical Phase-Shifters (EOPSSs) in each arm in a push-pull configuration. The EOPSSs are driven jointly to produce the four required amplitude levels ( $\mu_0, \mu_0/2, \mu_0/4, \emptyset$ ) for the 1-decoy BB84 protocol. Additionally, TOPSs in each arm stabilize the IM operating point. Because Bob's setup is passive, these TOPSs also provide the active phase compensation required to maintain stable interference at the receiver.

**Mean photon number setting:** A final EVOA combined with a MZI with TOPSs in both arms, attenuates the output to the desired mean photon number.

## B. Mitigating Chromatic Dispersion Without Dispersion Compensating Fibers

To assess the impact that halving the system's repetition rate had on chromatic dispersion sensitivity, we simulated the pulse broadening through a standard single-mode fiber with a dispersion parameter of 17.0ps/(nm·km)<sup>8</sup>. For an ideal Fourier-limited pulse of 40ps Full Width Half Maximum (FWHM) (our laser's temporal width - see Fig. 3b), the pulse width remains comfortably within the 400ps time bin even beyond 250km: 85ps at 50km, 150ps at 100km, and 300ps at 200km (solid line in Fig. 3a).

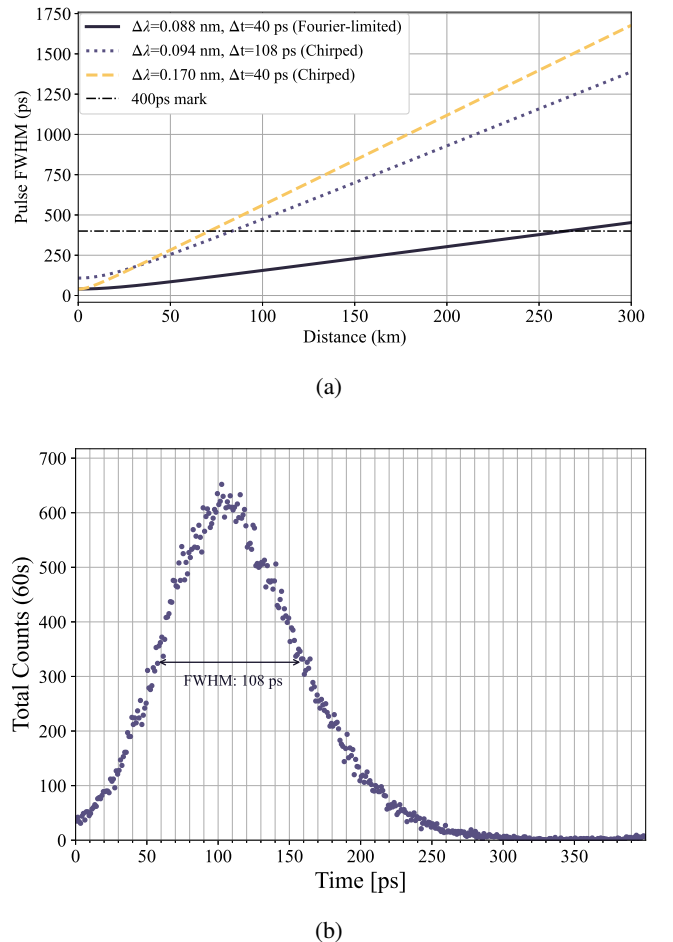


Figure 3: a) Simulated pulse broadening due to chromatic dispersion effects, based on measured laser parameters [except the calculated *Fourier-limited* scenario]. The 400 ps horizontal line indicates the time-bin width. The labels () indicate the function used for each curve. The frequency linewidth was measured using the same method as the ring filter in II A. b) Time-resolved intensity profile of the signal pulses measured with a SNSPD (50ps jitter) and a Time-to-Digital Converter (TDC) (ID100 in high-resolution mode (1ps resolution))

However, the experimental characterization of our laser revealed significant frequency chirp, causing the measured spectral width (0.170nm) to exceed the Fourier-limited value. To account for this chirp in our dispersion analysis, we use the modified broadening equation<sup>9</sup>:

$$T_1(z) = T_0 \left[ \left( 1 + \left( \frac{C \cdot z}{L_D} \right) \right)^2 + \left( \frac{z}{L_D} \right)^2 \right]^{\frac{1}{2}}, \quad (1)$$

where  $T_0$  is the initial pulse FWHM,  $T_1(z)$  is the broadened pulse width after distance  $z$ ,  $L_D = T_0/\beta_2$  is the dispersion length (with  $\beta_2$  being the group velocity dispersion parameter), and  $C$  is the chirp parameter determined from the measured spectral and temporal widths via  $2\pi c/\lambda_0^2 \cdot \Delta\lambda =$

$$(1 + C^2)^{1/2} / T_0$$

with  $\Delta\lambda$  being the spectral FWHM. Using Equation 1 with the measured parameters of our laser we obtained the dashed line in Fig. 3a. This reveals that at 100km, the pulse width would significantly exceed the 400ps time bin, resulting in an overlap with adjacent time-bins and high Quantum Bit Error Rate (QBER) values that would prevent key generation. To extend the system's maximum operating distance, we optimized the laser parameters by tuning the bias current and RF driving voltage to narrow the spectral width at the expense of increasing the temporal width. With a spectral width of 0.094 nm and a temporal width of 108ps FWHM (dotted line in Fig. 3a) we achieved operation at up to 105km without DCF, as demonstrated in Section IV.

### III. RECEIVER PROTOTYPE

The receiver unit consists of five layers: the integrated PIC comprising the optical components (except detectors); two single photon detectors, one for each measurement basis; a control PCB for thermal regulation, detector biasing, and signal readout; an FPGA for real-time data acquisition and classical communication with the transmitter; and a computer for post-processing tasks including error correction and privacy amplification. The computer also interfaces with a microcontroller-based current supply for the receiver PIC's tunable beam splitter, implemented using an operational amplifier in a current-sensing feedback configuration.

For a compact, deployable system, we sought a Peltier-cooled Negative Feedback Avalanche Diodes (NFADs) solution. While SNSPDs operating at cryogenic temperatures achieve excellent noise performance, they require bulky cryogenic systems, are mechanically complex and costly, making them unsuitable for our application. We initially evaluated pre-packaged, free-running NFADs from Wooriro Co. Ltd. with internal three-stage TECs (cooling to  $-50^{\circ}\text{C}$ ), but they exhibited high timing jitter ( $>400\text{ps}$ ) and Dark Count Rates (DCRs) ( $>1\text{kHz}$ ), requiring  $100\mu\text{s}$  dead times that limited count rates and restricted transmission distance. Full characterization is available in<sup>10</sup>. Given the limitations mentioned, we reverted to using legacy Princeton NFADs, peltier-cooled to  $-50^{\circ}\text{C}$ , for the field deployment. Despite their discontinuation, these detectors, to our knowledge, still offer the best jitter and noise performance among semiconductor single-photon detectors.

#### A. Integrated Receiver

It is crucial to have a low-loss receiver in order to achieve high key generation rates and not sacrifice the maximum transmission distance. Therefore, with this loss budget in mind, the PIC was fabricated through Femtosecond Laser Micromachining (FLM) in borosilicate glass (see Fig. 4), where tightly focused ultrashort pulses directly write waveguides inside the substrate<sup>11</sup>. This platform offers low insertion losses and intrinsic polarization insensitivity, ensuring that the device performs identically for any input polarization state, a

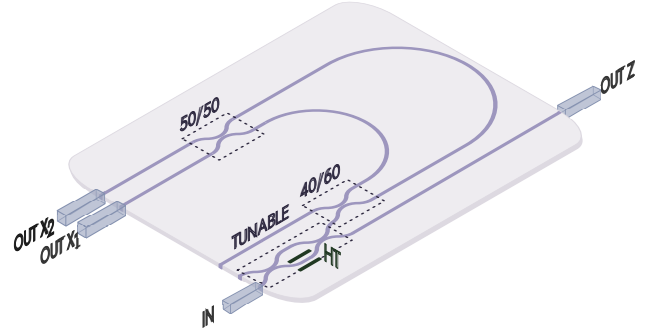


Figure 4: Schematic of the receiver's photonic integrated circuit, showing the optical signal path. HT - heater, OUT X<sub>n</sub> - output connected to X basis detector, OUT Z - output connected to Z basis detector. 40/60 and 50/50 refer to the splitting ratio of the interferometer's input and output coupler respectively.

feature essential for our protocol. Because photons travel through optical fibers, where birefringence causes random polarization changes, the device must operate reliably without requiring additional polarizing components, which would otherwise introduce extra losses. FLM naturally enables this: directional couplers exhibit polarization-independent splitting ratios, and the residual birefringence is both very small and tunable. It can be adjusted dynamically via temperature or permanently by inscribing stress tracks near the core with the same femtosecond laser<sup>12-14</sup>, exploiting the stress-optic effect. This tunability provides a degree of control not readily achievable in other platforms. Although FLM offers less miniaturization than standard lithographic technologies, it provides high modularity, true 3D routing, and low-loss photonic circuits. The laser-written waveguides are well matched to optical fibers in both mode size and refractive index profile, enabling efficient fiber-to-chip coupling. In this work, the waveguides are optimized for 1550nm.

Fig.4 shows the schematic of the receiver's PIC that can be divided into two main blocks one for basis selection and one for state measurement.

**Basis selection:** A tunable BS is used to set the measurement basis splitting ratio. The tunable BS is implemented as a MZI, with a microheater placed on one arm to enable thermo-optic phase tuning. The microheater is fabricated by patterning the resistor via selective femtosecond laser ablation of a 100 nm Cr/Au film previously deposited on the substrate<sup>15</sup>. The splitting ratio can be continuously tuned from 0 to 100% in the X basis by applying a 63mA to the microheater.

The tunable BS provides two key advantages: it enables optimization of basis selection probabilities for different channel losses, making a single receiver design suitable for varied deployment scenarios; and it eliminates the need for multiple specialized chip designs during fabrication, reducing production complexity and cost while improving scalability.

**State measurement:** The receiver MZI performs an interferometric measurement of the time-bin qubits. The MZI has a 0.01ps path length mismatch with Alice. To ensure balanced interference, the MZI's input directional coupler has a 40/60 splitting ratio to pre-compensate for the loss asymmetry arising from the path length difference. Ideally, this would fully correct the amplitude difference, but due to technical imperfections, a residual 2.5% mismatch remains. A minimum visibility of 99.73% (under the worst incoming polarization state was measured with the PIC's temperature stabilized at 14.2°C). The visibility's contribution to the  $QBER_X$  is given by  $\frac{1-V}{2}$  and its impact is negligible in these operating conditions.

Light is butt coupled in and out of the chip and the total optical loss (taking coupling into account) is measured to be 2.17dB in the **Z** basis and 3.52dB in the **X** basis. Despite having an interferometer twice as long as the one reported by Sax<sup>7</sup>, the low-loss nature of the FLM-written waveguides in borosilicate glass, and the high coupling efficiency, ensure only a marginal 0.02 dB increase in loss within the X-basis arm.

#### IV. METROPOLITAN DEPLOYMENT AND RESULTS

To assess the viability of our system for real-world deployment, we characterized its performance in the Geneva metropolitan network, deploying it across 4.6km of installed Single Mode Fiber (SMF) (9.4dB total loss). The transmitter and receiver were located in two different University buildings connected by 4.6 km of installed fiber (9.4 dB total loss). Initially, the system was operated at  $-50^{\circ}\text{C}$  with standard Peltier cooling. An automatic feedback loop stabilized the relative phase between the transmitter and receiver by tuning the phase in the transmitter's MZI based on the measured value of the phase error rate ( $\phi_z$ ). This was implemented even though the stability of the MZIs pair exceeded 40 minutes without active stabilization, in anticipation of long term operation.

The experimental results and settings are summarized in Table I, Table II and Fig. 5. For error correction, we perform in real-time a Cascade algorithm with a block size of 8192 bits and 1.05 efficiency.

	$\mu_2$	$\mu_1$	$p_x$	$p_z$
Short Distances	0.50	0.26	0.2	0.80
Long Distances	0.50	0.26	0.34	0.66

Table I: Experimental parameters.  $\mu_0$  and  $\mu_1$  are the mean photon number of the signal and decoy states respectively and the ratios of sending  $x$  and  $y$  states are  $p_x$  and  $p_y$  respectively. Short Distances:  $\leq 30\text{km}$ ; Long Distances:  $\geq 30\text{km} \& \geq 35\text{dB}$ .

As shown in the first entry of Table II, we measured a Secret Key Rate (SKR) of 6.7 kbps with a  $\phi_z$  of only 2.0%. The robustness of the system was further validated by continuous operation over 12 day-and-night cycles without human intervention (Fig. 5). The system was still stable and fully operational when the experiment was terminated, indicating that the duration of the key exchange was limited only by our experimental schedule rather than by any inherent instability in the hardware or the phase compensation feedback loop. To explore the maximum distance achieved with our system, additional standard SMF spools were added at the receiving building, extending the link after the deployed fiber. Due to the high DCRs at  $-50^{\circ}\text{C}$  (approximately 2 kcps), the system QBERs were affected and the maximum secure transmission distance achieved was 59.8km.

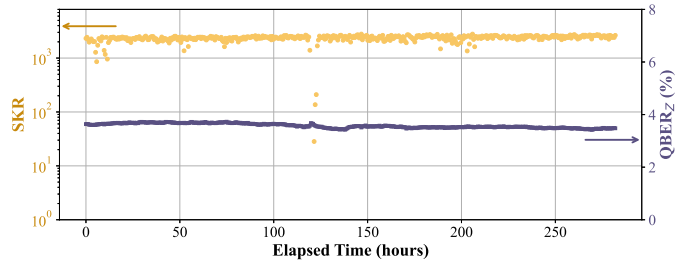


Figure 5: Stability of the SKR and  $QBER_Z$  over a 282h (around 12 days) measurement of a point-to-point key exchange in the deployed fiber link.

In order to assess the maximum achievable distance without DCF, and avoid being limited by the detectors' DCR, we transitioned to a Stirling-cooled regime at  $-85^{\circ}\text{C}$ . This significant reduction in noise (77 cps) allowed us to extend the key exchange distance up to 105.4km of SMF (Table II). It should be noted that the use of a Stirling cooler does not necessarily compromise the portability or integration of the system in metropolitan networks, as modern miniature Stirling units (micro-coolers) offer a compact footprint comparable to some Peltier assemblies while providing superior cooling power to reach the low-noise regime of semiconductor detectors.

To distinguish the fundamental loss limitation of our system from chromatic dispersion effects, we characterized the loss-dependent performance by adding a Variable Optical Attenuator (VOA) to the metropolitan link (last two entries of Table II). The system maintains good performance up to 35dB, with  $q_z$  remaining below 2% and achieving a SKR of 0.90 kbps. Even with 40dB attenuation, our system managed a key extraction with a SKR of 0.16 kbps. However, at this attenuation level the signal count rate becomes comparable to the detector dark count rate, pushing the system into a DCR limited regime. This is evidenced by the sharp increase in  $\phi_z$  from 6.0% at 35dB to 13.6% at 40dB. This establishes approximately 40dB as the maximum loss budget of our system in the absence of dispersion, beyond which the dark counts prevent positive key extraction. Comparing these VOA results with the long-distance fiber measurements reveals the significant impact of chromatic dispersion. Despite experiencing 6.6

Quantum Channel		Detectors					Distillation		Performance			
L (km)	Att (dB)	$\eta_{data}$ (%)	$\tau_{data}$ (μs)	$\eta_{mon}$ (%)	$\tau_{mon}$ (μs)	T (° C)	$p_X^{(B)}$	n	$t_{ccp}$ (s)	$q_z$ (%)	$\phi_z$ (%)	SKR (kbps)
4.6	9.4	20	6	20	7	-50	0.50	$8 \times 10^6$	$7.2 \times 10^3$	3.3	2.0	6.7
59.8	17.0	20	6	20	7	-50	0.50	$8 \times 10^6$	$1.7 \times 10^5$	9.7	9.9	0.8
17.3	12.0	19	1	19	3	-85	0.10	$8 \times 10^6$	$1.6 \times 10^3$	1.9	3.6	13.2
29.9	14.9	21	3	20	7	-85	0.10	$8 \times 10^6$	$2.0 \times 10^3$	2.5	3.8	9.8
59.8	17.0	21	3	20	7	-85	0.10	$8 \times 10^6$	$3.3 \times 10^3$	2.9	5.1	5.6
105.4	33.4	21	6	20	8	-85	0.35	$8 \times 10^4$	$1.8 \times 10^3$	7.4	10	0.3
4.6	35	21	6	20	7	-85	0.1	$8 \times 10^6$	$1.7 \times 10^4$	1.3	6.0	0.9
4.6	40	19	2	20	27	-85	0.4	$1 \times 10^4$	$6.7 \times 10^4$	3.3	13.6	0.16

Table II: Experimental parameters and performance metrics for the metropolitan link with varying total fiber lengths. All measurements were performed on an installed metropolitan network, with additional standard SMF spools used to evaluate system performance at extended distances [2-6], or extra attenuation [7-8]. The data highlights the transition from Peltier cooling at  $-50^{\circ}\text{C}$  to Stirling cooling at  $-85^{\circ}\text{C}$  to overcome DCR limitations at higher attenuation.  $L$  refers to the Quantum Channel (QC) length,  $Att$  to the total attenuation in the QC,  $\eta_x$  and  $\tau_x$  refer to the efficiency and dead time, respectively, of the *data* and *monitor* detectors used.  $T$  is the detector's operating temperature, and  $p_X^{(B)}$  denotes Bob's probability of measuring in the  $X$  basis.  $n$  and  $t_{ccp}$  are the raw key block size and acquisition time respectively,  $q_z$ ,  $\phi_z$  and  $SKR$  denote the QBER in the  $Z$  basis, phase error rate and Secret Key Rate.

dB more loss, the VOA configuration exhibits a  $q_z$  more than  $2 \times$  lower, demonstrating that chromatic dispersion becomes the dominant performance limitation at longer distances.

Looking into the trade-off between raw repetition rate (2.5GHz in<sup>7</sup> and 1.25GHz in this work) and key quality, we observed consistently lower QBER values compared to those reported by<sup>7</sup> for similar attenuation levels. Comparing the performance at 30dB, our system achieved a  $q_z$  of 1.3% and an SKR of 1.80 kbps, whereas the system in<sup>7</sup>, despite doubling our repetition rate, demonstrated a SKR of 2.9 kbps with a significantly higher QBER of 3.6%. This trend of high-quality key extraction continues through higher attenuation levels. This demonstrates that for many practical fiber links, optimizing for a low QBER floor with a moderate repetition rate is a more effective strategy for secret key extraction than simply increasing pulse frequency. This is especially true for systems deployed in short distance links, where detector saturation is already expected. Notably, although longer interferometers are generally less stable, our unbalanced MZI remained stable for over 40 min without the use of stabilization loops.

## V. CONCLUSION

In this work, an integrated photonics based QKD prototype has been successfully deployed in a metropolitan network. By integrating all components into optical chips (except the laser and detectors) and consolidating the totality of the QKD transmitter and receiver into standard 19-inch racks, we demonstrated a stable, real-world architecture ca-

pable of autonomous key exchange. This demonstration reinforces the maturity of chip-based QKD for practical use. By offering compact, scalable and stable architectures these platforms can streamline the implementation of quantum security within standard telecommunications networks.

## VI. ACKNOWLEDGMENTS

We gratefully acknowledge Sicoya GmbH for manufacturing the photonic integrated chip used in the transmitter's setup. We thank ID Quantique for providing the chassis, PC/FPGA system for Alice. We thank Claudio Barreiro and for his contributions to the PCB design work and David Cabrerizo for helping with the PCB assembly.

## REFERENCES

- 1 S. Pirandola, U. L. Andersen, L. Banchi, M. Berta, D. Bunandar, R. Colbeck, D. Englund, T. Gehring, C. Lupo, C. Ottaviani, J. L. Pereira, M. Razavi, J. Shamsul Shaari, M. Tomamichel, V. C. Usenko, G. Vallone, P. Villoresi, and P. Wallden, "Advances in quantum cryptography," *Adv. Opt. Photonics* **12**, 1012 (2020).
- 2 F. Xu, X. Ma, Q. Zhang, H.-K. Lo, and J.-W. Pan, "Secure quantum key distribution with realistic devices," *Rev. Mod. Phys.* **92**, 025002 (2020).
- 3 L. Labonte, O. Alibart, V. DAuria, F. Doutre, J. Etesse, G. Sauder, A. Martin, E. Picholle, and S. Tanzilli, "Integrated photonics for quantum communications and metrology," *PRX quantum* **5**, 010101 (2024).
- 4 A. Boaron, B. Korzh, R. Houlmann, G. Bosso, D. Rusca, S. Gray, M. J. Li, D. Nolan, A. Martin, and H. Zbinden, "Simple 2.5 ghz time-bin quantum key distribution," *Applied Physics Letters* **112** (2018), 10.1063/1.5027030.

<sup>5</sup>D. Rusca, A. Boaron, F. Grunenfelder, A. Martin, and H. Zbinden, “Finite-key analysis for the 1-decoy state qkd protocol,” *Applied Physics Letters* **112**, 171104 (2018).

<sup>6</sup>D. Rusca, A. Boaron, M. Curty, A. Martin, and H. Zbinden, “Security proof for a simplified bennett-brassard 1984 quantum-key-distribution protocol,” *Phys. Rev. A* **98**, 052336 (2018).

<sup>7</sup>R. Sax, A. Boaron, G. Boso, S. Atzeni, A. Crespi, F. Grunenfelder, D. Rusca, A. Al-Saadi, D. Bronzi, S. Kupijai, H. Rhee, R. Osellame, and H. Zbinden, “High-speed integrated qkd system,” *Photon. Res.* **11**, 1007–1014 (2023).

<sup>8</sup>R. Ramaswami, K. N. Sivarajan, and G. H. Sasaki, “chapter 5 - transmission system engineering,” in *Optical Networks (Third Edition)*, edited by R. Ramaswami, K. N. Sivarajan, and G. H. Sasaki (Morgan Kaufmann, Boston, 2010) third edition ed., pp. 289–365.

<sup>9</sup>G. Agrawal, *Nonlinear fiber optics*, 6th ed. (Elsevier Academic Press, 2019).

<sup>10</sup>M. A. de Matos Afonso Pereira, *Towards Deployable Quantum Communication: Integrated Quantum Key Distribution and Randomness Generation*, Ph.D. thesis, Université de Genève (2026).

<sup>11</sup>G. Corrielli, A. Crespi, and R. Osellame, “Femtosecond laser micromachining for integrated quantum photonics,” *Nanophotonics* **10**, 3789–3810 (2021).

<sup>12</sup>L. A. Fernandes, R. D. R. B. Layman, J. R. Grenier, and P. R. Herman, “Stress induced birefringence tuning in femtosecond laser fabricated waveguides in fused silica,” *Optics Express* **20**, 24103–24114 (2012).

<sup>13</sup>V. R. Bhardwaj, E. Simova, P. P. Rajeev, C. Hnatovsky, R. S. Taylor, D. M. Rayner, and P. B. Corkum, “Stress in femtosecond-laser-written waveguides in fused silica,” *J. Opt. Soc. Am. B* **21**, 191–198 (2004).

<sup>14</sup>B. McMillen, P. R. Herman, G. A. Torchia, P. Kazansky, and W. Watanabe, “Femtosecond laser direct-write waveplates based on stress engineered retardance,” *Optical Materials Express* **6**, 3865–3876 (2016).

<sup>15</sup>F. Ceccarelli, S. Atzeni, A. Prencipe, R. Farinaro, and R. Osellame, “Thermal phase shifters for femtosecond laser written photonic integrated circuits,” *Journal of Lightwave Technology* **37**, 4275–4282 (2019).